

Interlayer coupling rotatable magnetic easy-axis in MnSe₂ mono- and bi-layers

Zhongqin Zhang^{1,2,3,†}, Cong Wang^{2,3,†,*}, Peng-Jie Guo^{2,3}, Linwei Zhou^{2,3}, Yuhao Pan^{2,3,4,5}, Zhixin Hu^{1,*} and Wei Ji^{2,3,*}

¹*Center for Joint Quantum Studies and School of Physics, Tianjin University, Tianjin, China*

²*Beijing Key Laboratory of Optoelectronic Functional Materials & Micro-Nano Devices, School of Physics, Renmin University of China, Beijing 100872, China*

³*Key Laboratory of Quantum State Construction and Manipulation (Ministry of Education), Renmin University of China, Beijing 100872, China*

⁴*China North Artificial Intelligence & Innovation Research Institute, Beijing 100872, China*

⁵*Collective Intelligence & Collaboration Laboratory, Beijing 100872, China*

*Emails: wcphys@ruc.edu.cn (C.W), zhixin.hu@tju.edu.cn (Z.H.), wji@ruc.edu.cn (W.J.)

Interlayer coupling plays a critical role in tuning the electronic structures and magnetic ground states of two-dimensional materials, influenced by the number of layers, interlayer distances, and stacking order. However, its effect on the orientation of the magnetic easy axis remains underexplored. In this study, we demonstrate that interlayer coupling can significantly alter the magnetic easy-axis orientation, as shown by the magnetic easy-axis of monolayer 1T-MnSe₂ tilting 67° from the *z*-axis, while aligning with the *z*-axis in the bilayer. This change results from variations in orbital occupations near the Fermi level, particularly involving nonmetallic Se atoms. Contrary to the traditional focus on magnetic metal atoms, our findings reveal that Se orbitals play a key role in influencing the easy-axis orientation and topological Chern numbers. Furthermore, we validated our conclusions by changing stacking orders, introducing charge doping, applying in-plane biaxial strains, and substituting non-metallic atoms. Our results highlight the pivotal role of interlayer coupling in tuning the magnetic properties of layered materials, with important implications for spintronic applications.

I. INTRODUCTION

Two-dimensional (2D) van der Waals (vdW) magnetic materials have garnered significant attention and have achieved notable advancements in recent years [1,2], emerging as a promising platform for both fundamental research [3,4] and potential spintronics applications [5,6]. The magnetic properties of these materials are typically characterized by magnetization [7–9], magnetic orders [2,10,11] and magnetic anisotropy [10,12,13], with the latter two being easily tunable. Extensive discussions have been conducted on both in-plane and out-of-plane magnetic orders, associated net magnetization values, and their manipulation mechanisms for 2D magnets. In addition to these properties, magnetic anisotropy plays a pivotal role in sustaining long-range magnetic orders in 2D magnets at finite temperatures [3,4]. It is also closely associated with magnetic coercivity, a critical parameter determining whether the material behaves as a hard or soft magnet [14–16]. However, results on the magnetic easy-axis are, unlike the magnetic order, available only for a limited number of 2D magnets, such as CrTe₂ [10]. This limitation in understanding hinders us to grasp the factors that could affect magnetic anisotropy, thereby limiting the development of effective strategies for modulating magnetic anisotropy.

The magnetic anisotropy was demonstrated to be tunable under various external stimuli, such as electric fields [17–19] and charge doping [20,21], which primarily change the filling of *d* orbitals of magnetic metal atoms. However, such tunability typically requires high stimulating strengths, which can lead to magnetic order transitions [22,23] or irreversible structural phase transitions [24,25]. Thus, it is of paramount importance to explore gentle and sustainable mechanisms for rotating the magnetic easy axis direction without introducing transitions of magnetic order or atomic structures. The ability to modulate various properties through interlayer coupling is one of the most striking features of 2D materials [19]. In 2D magnets, many demonstrations highlight the role of interlayer coupling in manipulating interlayer or intralayer magnetic order [28–32]. Although the orientation of the magnetic easy-axis was observed to vary upon changing the number of layers in 1T-CrTe₂ [33,34] and

alpha-RuCl₃ [35]. However, these systems also exhibit synchronous magnetic order transition [33,34] or structural symmetry-breaking [35] with layer number variation. The question of whether interlayer coupling can tune magnetic anisotropy independently remains largely unexplored.

In this article, we theoretically explored the ability and mechanism to tune the magnetic easy axis in prototypic MnSe₂ mono- and bi-layers via interlayer coupling using density functional theory (DFT) calculations. We found that the magnetic easy-axis rotates from 67° off the z -axis in the monolayer to the z -axis in the bilayer, without any transition of magnetic orders or atomic structures. By analyzing the contribution of each individual atom and orbital to the MAE, we identified that the electron occupation of Se p orbitals is critical in driving this rotation. A comparison of the electronic band structures of the mono- and bi-layers reveals the mechanism behind the occupation changes and the subsequent magnetic easy-axis rotation through interlayer electronic couplings upon stacking. This mechanism was further validated by tuning the occupation using other external stimuli such as stacking order changes, electron or hole doping, in-plane biaxial strains and substitution of non-metallic atoms. Additionally, we observed that the Chern number of electronic bands near the Fermi level varies in response to the rotating magnetic moments and/or layer stacking, demonstrating ability to manipulate topological properties of these electronic states through various external stimuli.

II. METHODS

Our density functional theory (DFT) calculations were performed using the generalized gradient approximation (GGA) for the exchange correlation potential in the form of PerdewBurke–Ernzerhof (PBE) [39], the projector augmented wave method [40], and a plane-wave basis set as implemented in the Vienna ab-initio simulation package (VASP) [41]. We also included the dispersion correction through Grimme’s semiempirical D3 scheme [42] in combination with the PBE functional (PBE-D3). This combination yields accuracy comparable to that of the optB86b-vdW

functional for describing geometric properties of layered materials(Appendix A) [43], but at a lower computational cost. The MAE in MnSe₂ is on the order of 0.1 meV, and during the relaxation of the volume and lattice shape, the Pulay stress issue was also encountered. Therefore, to accurately compute the atomic structures, electronic structure, and MAE, kinetic energy cutoffs of 800 and 600 eV for the planewave basis were adopted for structural relaxations and electronic structure calculations, respectively. All atoms, lattice volumes, and shapes were allowed to relax until the residual force per atom was below 0.01 eV/Å. A vacuum layer exceeding 15 Å in thickness (22 Å for the monolayers and 18 Å for the bilayers) was employed to reduce imaging interactions between adjacent supercells. A Gamma-centered k -mesh of $21 \times 21 \times 1$ was used to sample the first Brillouin zone of the unit cell for MnSe₂. The Gaussian smearing method with a σ value of 0.01 eV was applied for structural relaxation and electronic structure calculations. To accurately calculate the MAE, the tetrahedron method with Blöchl corrections and a Gamma-centered k -mesh of $29 \times 29 \times 1$ was used. The on-site Coulomb interaction for Mn d orbitals was characterized by U and J values of 4.0 eV and 0.7 eV [44], respectively, as determined via a linear response method [45] and validated by the convergence of theoretical predictions(Appendix A). A $2 \times 2\sqrt{3}$ supercell and four (eight) magnetic configurations (Appendix B) were considered to identify the magnetic ground state for the monolayer (bilayer). Spin-exchange coupling parameters were extracted based on an anisotropic nearest-neighbor Heisenberg model; please refer to Appendix C for details.

The Atomic-orbital Based Ab-initio Computation at USTC (ABACUS) package [46,47] and PYATB [48] were used to calculate the Chern numbers. By using the Wannier90 package, we constructed the tight-binding model of MnSe₂ with Mn $3d$ and Se $4p$ orbitals based on the maximally localized Wannier functions method (MLWF) [49]. We further plotted edge states and verified our conclusions regarding topological transitions using the WannierTools software package [50].

Direct charge doping was applied to Se atoms using the ionic potential method [51]. Specifically, electrons (or holes) were extracted from a $3d$ core level of

Se and placed into the lowest unoccupied band of MnSe₂. This method ensures that the doped charges remain localized around the Se atoms while maintaining the neutrality of the layer. In-plane biaxial strain was simulated on the monolayer MnSe₂, which was fully relaxed in the ferromagnetic configuration. When biaxial strains were applied, the in-plane lattice vectors of the equilibrium configuration were compressed or stretched. The ferromagnetic configuration was used for structural relaxations and its superior stability was further verified by comparing its energy with another three magnetic configurations. For example, to model a -2% biaxial strain, the equilibrium in-plane lattice vectors were compressed from 3.61 Å to 3.54 Å (by 2%). In subsequent structural relaxations, all atoms are were allowed to move and the in-plane lattice constants are were kept fixed.

The spin-orbit coupling was considered in all calculations carried out to determine the magnetic easy-axis directions. The magnetic easy-axis was identified using the Renmin Magnetic Easy Axis Finder (ReMEAF) toolkit [52], which utilizes the simulated annealing algorithm and invokes VASP to determine the global easy-axis orientation. In angular dependence of MAE, for the area between calculated points, we used linear interpolation to give MAE values.

Spin-exchange coupling parameters were extracted based on Heisenberg model as follow:

$$H = H_0 - J_1 \sum_{\langle i \neq j \rangle} \vec{S}_i \cdot \vec{S}_j - J_2 \sum_{\langle\langle i \neq j \rangle\rangle} \vec{S}_i \cdot \vec{S}_j - J_3 \sum_{\langle\langle\langle i \neq j \rangle\rangle\rangle} \vec{S}_i \cdot \vec{S}_j \\ - J_4 \sum_{\langle i, j \rangle} \vec{S}_i \cdot \vec{S}_j - J_5 \sum_{\langle\langle i, j \rangle\rangle} \vec{S}_i \cdot \vec{S}_j - J_6 \sum_{\langle\langle\langle i, j \rangle\rangle\rangle} \vec{S}_i \cdot \vec{S}_j$$

Here, $J_1 \sim J_3$ and $J_4 \sim J_6$ represent the three nearest intra- and interlayer couplings, respectively, as illustrated in Fig. 1(a)~(c). Here, the method for extracting the exchange constants J_1 , J_2 , and J_3 in the monolayer is presented, and that for the bilayer can be found in Appendix B. First, we wrote the expressions of the Heisenberg model for different magnetic configurations shown in Fig. 6 a-d:

$$E_a = -\frac{N^2}{4} \times \frac{1}{2} (6J_1 + 6J_2 + 6J_3) + E_0$$

$$\begin{aligned}
E_b &= -\frac{N^2}{4} \times \frac{1}{2} (2J_1 - 2J_2 - 2J_3) + E_0 \\
E_c &= -\frac{N^2}{4} \times \frac{1}{2} (-2J_1 - 2J_2 + 6J_3) + E_0 \\
E_d &= -\frac{N^2}{4} \times \frac{1}{2} (-2J_1 + 2J_2 - 2J_3) + E_0
\end{aligned}$$

where N represents the unpaired spins on each Mn atom, which is treated as 3 in our exchange parameter calculations and E_0 represents the energy that is independent of the magnetic configuration. Then, by substituting the energies of the magnetic configurations from Table 5, we solved for the values of the exchange constants.

III. RESULTS AND DISCUSSIONS

A. Magnetic anisotropy in MnSe₂ monolayer and bilayer

Monolayer MnSe₂ crystallizes in a hexagonal $1T$ structure with space group $P\bar{3}m1$, as depicted in Fig. 1a. Each Mn atom is octahedrally coordinated by six Se atoms, with Se-Mn-Se bond angle close to 90° (measured as either 90.96° or 89.04°), indicating minimal Jahn-Teller distortion. In the MnSe₂ bilayer, the AA stacking (Fig. 1b and 1c) is found to be over 4 meV/Mn more stable compared to other stacking configurations (Appendix D). To determine intra- and interlayer magnetic ground state, we adopted same structure using the optimized structures with the ferromagnetic (FM) order and calculated relative energies of four (eight) magnetic configurations for monolayer (bilayer) MnSe₂ (see Appendix B for more details). We found that both the monolayer and the bilayer exhibit a FM ground state, as indicated by the data listed in Table 5, consistent with the theoretical predictions reported in the literature [28,53].

Three intra-layer (J_1 to J_3) and three inter-layer (J_4 to J_6) spin-exchange coupling parameters, which are indicated by dashed arrows in different colors in Fig. 1a-1c, were computed based on the Heisenberg model (seen in II. METHODS and Appendix B), , with their values provided in Table 1. Notably, the dominant and positive nearest-neighbor intralayer spin-exchange coupling J_1 (7.5 and 8.7 meV/Mn for the mono- and bi-layer) aligns with the energetically favored intralayer FM configuration. Comparable

values for the interlayer spin-exchanges, $J_4=3.6$ meV/Mn and $J_5=3.5$ meV/Mn, indicate that the interlayer FM coupling is as strong as the intra-layer magnetic coupling in MnSe₂, which is prominent in layered magnetic materials [29,43,54].

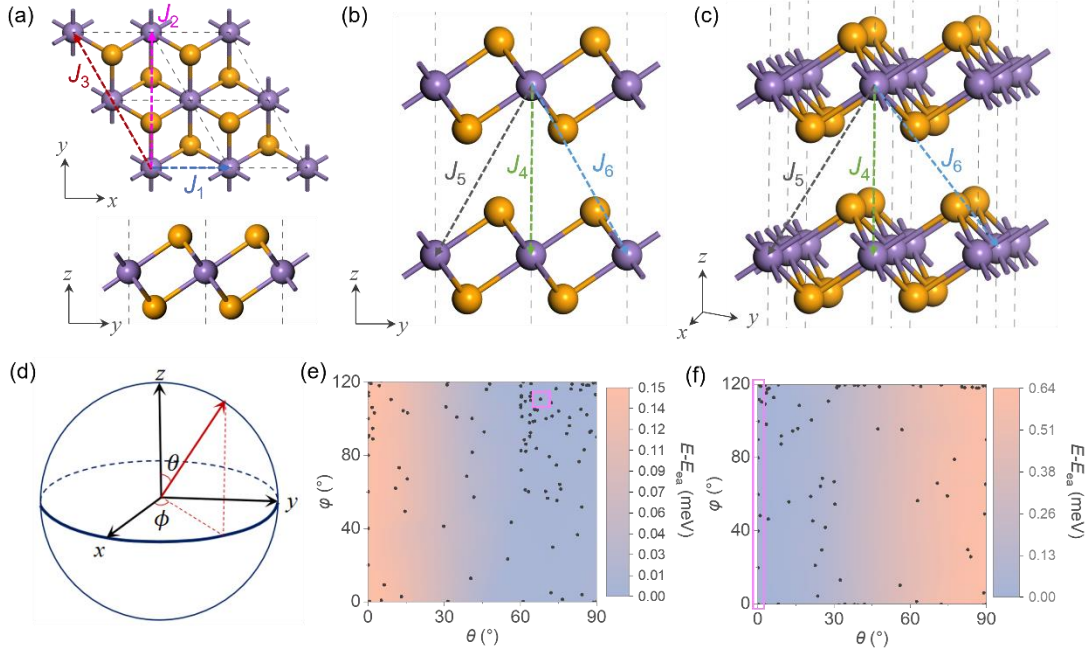


Fig. 1. Structure and easy axis of mono- and bilayer MnSe₂. (a) Top and side views of monolayer MnSe₂. Purple and orange balls represent Mn and Se atoms, respectively. Dashed arrows denote intralayer spin-exchange parameters J_1 , J_2 and J_3 between Mn sites with different colors. (b-c) Side and oblique view of an AA-stacked bilayer MnSe₂. Colored dashed arrows denote interlayer spin-exchange parameters J_4 , J_5 and J_6 between Mn sites. (d) Definition of polar angle θ and azimuth angle ϕ in the spherical coordinate. (e-f) Angular dependence of the calculated MAE of monolayer(e) and bilayer(f) MnSe₂. The total energy of the Mn moment oriented to the direction of easy axis was chosen as the zero-energy reference and marked by pink boxes. Black dots represent MAE results for angles calculated with DFT.

Table 1. Lattice constant, magnetic ground state, exchange parameters and easy axis of MnSe₂. Magnetic Anisotropy Energy (MAE) is defined as the energy difference required to reorient the magnetic moment of MnSe₂ from its easy axis to hard axis.

Layer Number	Lattice Constant (Å)	Mag. Config.		Exchange Parameters (meV/Mn)						Easy Axis		MAE (meV/Mn)
		Intralayer	Interlayer	J_1	J_2	J_3	J_4	J_5	J_6	$\theta(^{\circ})$	$\varphi(^{\circ})$	
1L	3.61	FM	-	7.5	1.2	0.2	-	-	-	67	111	0.2
2L	3.63	FM	FM	8.7	0.3	1.0	3.6	3.5	0.7	0	-	0.6

By considering the C_{3v} spatial symmetries inherent in $MnSe_2$, a range of polar angle $\theta \in [0, 90^{\circ}]$ and azimuth angle $\varphi \in [0, 120^{\circ}]$ (Fig. 1d) covers all possible magnetic easy-axis orientations. Figure 1e plots the magnetic anisotropic energies of the $MnSe_2$ monolayer where its magnetization direction rotates as a function of θ and φ , revealing an easy axis orientation along $\theta=67^{\circ}$ and $\varphi=111^{\circ}$. When an additional layer is stacked onto the monolayer to form the bilayer, the easy axis rotates to align with the z -axis ($\theta=0$, Fig. 1f). Such a substantial rotation of the magnetic easy-axis direction by adding a single layer to a monolayer has yet to be reported in 2D layered magnetic materials and warrants further exploration.

B. Origin of the interlayer coupling tunable magnetic easy-axis direction

Figure 2a shows the interlayer differential charge density of the bilayer $MnSe_2$. Apparent charge reduction (blue contours) near the interlayer Se atoms (pink balls) and charge accumulation mainly in the vdW gap region (light yellow contours) suggest strong interlayer electronic hybridization. Meanwhile, charge transfer on Mn and surface Se (orange balls) is less significant, indicating a weaker effect of interlayer coupling on them and thus a different contribution to the easy-axis rotation. To understand the role of interlayer coupling in rotating the easy axis, we decomposed the MAE contribution into individual atoms (Fig. 2b). Here, positive and negative MAE contributions correspond to magnetic easy-axis directions tending towards the z -axis and in-plane directions, respectively. In the $MnSe_2$ monolayer, all Se atoms are categorized as Se-surface atoms and contribute a positive value (0.36 meV/atom) to the MAE, while Mn atoms donate a smaller negative contribution (-0.04 meV/atom) to the MAE, favoring an in-plane magnetic easy-axis. The competition between these contributions results in the tilted orientation of the magnetic easy-axis in the monolayer. After the stacking of an additional $MnSe_2$ layer, the MAE contributions for Mn and

surface Se atoms change sign but have smaller absolute values (no more than 0.25 meV/atom). However, the Se-interface atoms exhibit a dominant positive MAE contribution (1.58 meV/atom), decisively outweighing the negative contribution from Se-surface (-0.25 meV/atom), leading to the alignment of the magnetic easy axis with the z -axis in the bilayer.

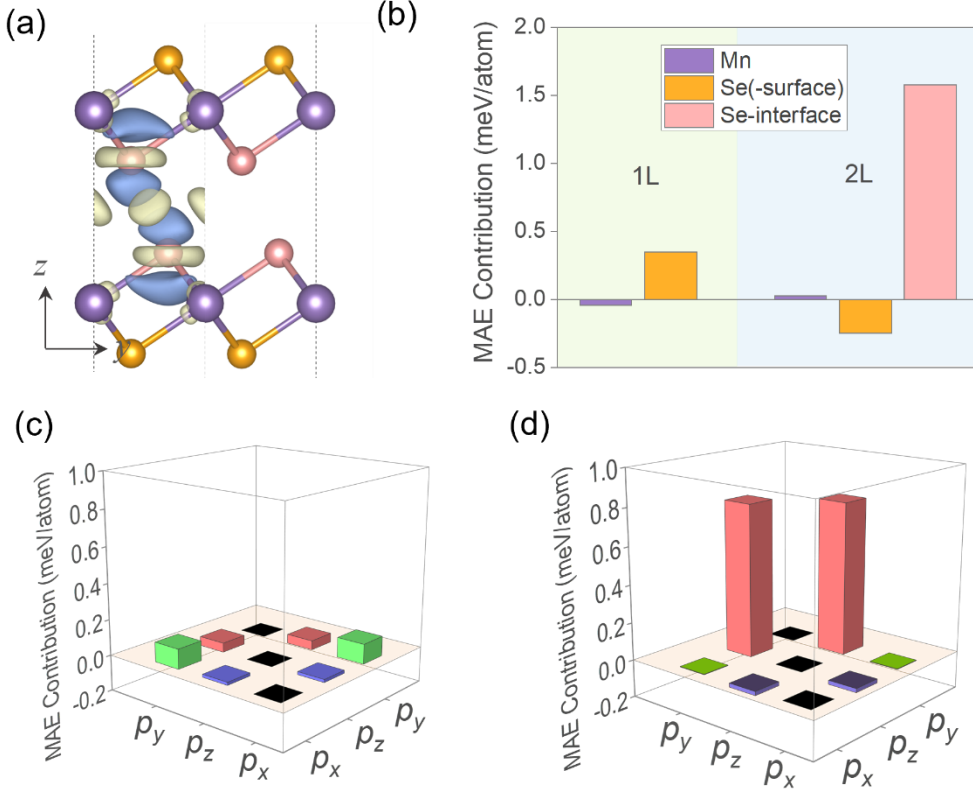


Fig. 2 (a) Side view of interlayer differential charge density (DCD) of bilayer MnSe₂ with an isosurface value of 0.0005 e/Bohr^3 . Light yellow and blue isosurface indicates charge accumulation and reduction after layer stacking. Non-equivalent Se atoms in bilayer MnSe₂ are colored in orange and pink. (b) Atomically decomposed MAE contributions of monolayer(1L) and bilayer(2L) MnSe₂. (c-d) Orbital-resolved MAE contributions of Se in monolayer(c) and Se-interface in bilayer(d).

Therefore, we further focused on the origin of the different Se contributions to MAE across different numbers of layers and decomposed the MAE into Se p_x , p_y , and p_z orbitals for the mono- (Fig. 2c) and bi-layer (Fig. 2d), namely:

$$\langle p_i | H_{\text{SOC}}(x) | p_j \rangle - \langle p_i | H_{\text{SOC}}(z) | p_j \rangle$$

where $H_{\text{SOC}}(x)$ is the spin-orbit coupling Hamiltonian when the magnetic moment is oriented along the x -direction, and the p_i, p_j represents p_x, p_y or p_z . In the monolayer, all Se orbital contributions are relatively small, resulting in the moderate total contribution of 0.36 meV/atom. As for the bilayer, the contribution from the p_z - p_y component of Se-interface atoms (~ 0.8 meV/atom) is significantly prominent and at least an order of magnitude larger than other components (less than 0.03 meV/atom). This result indicates that the interaction between the p_z and p_y orbitals of the Se-interface atoms is crucial in orienting the magnetic easy-axis toward the normal direction in the MnSe₂ bilayer. This finding provides a different perspective from the prevailing view in the literature, which attributes easy-axis reorientation due to interlayer couplings primarily to the influence of metallic atoms.

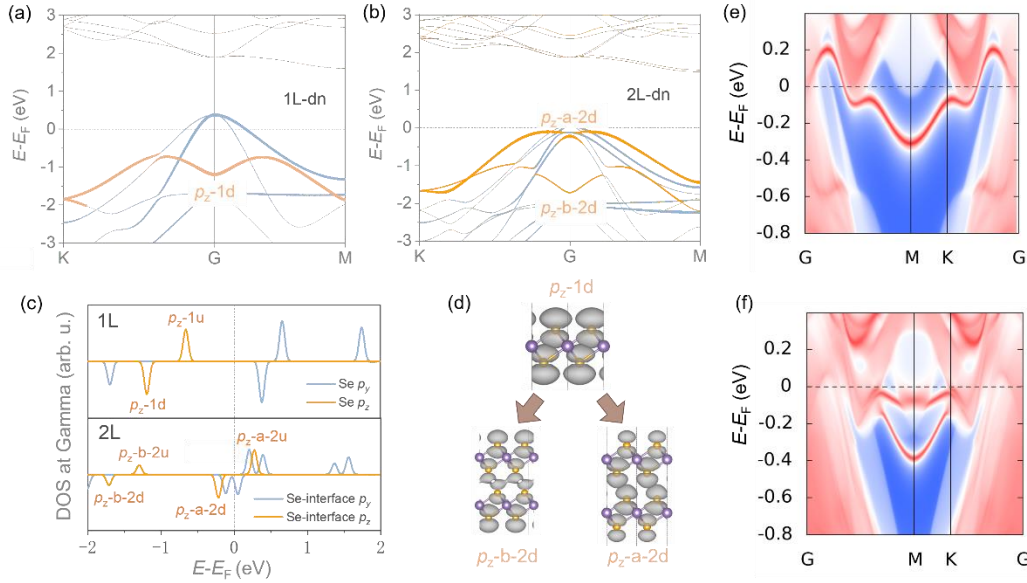


Fig. 3 Electronic structures of MnSe₂. (a-b) Spin-down band structures of monolayer(a) and bilayer(b) MnSe₂. The p_z and p_y orbitals of (interfacial) Se are mapped with different colors in bands near the Fermi level: orange, p_z ; light blue, p_y . The Fermi level is marked using grey dot dash line. (c) Projected density of states for the p_y and p_z orbitals of (interfacial) Se at the Gamma point in monolayer (upper panel) and bilayer (lower panel). (d) Visualized wave-function norms for the labeled states in (a-c). The isosurface value is 0.0012 e/Bohr³. (e,f) Surface states of monolayer(e) and bilayer(f) MnSe₂.

To understand the origin of the pronounced p_z - p_y component, we mapped the orbitals of (interfacial) Se on the band structures of both monolayer and bilayer. The orbital decomposition and layer number dependence of electronic band structures show qualitative consistency with different spin components. For clarity, we examine the spin-down electronic structure here (Fig. 3a-b) and provide the details of spin-up results in the Appendix G. According to second-order perturbation theory [55], the states with different occupations near the Fermi level contribute most significantly to the MAE, primarily composed of p_z and p_y orbitals in both mono- and bilayer MnSe₂. For a clear comparison, we plot the projected density of states (PDOS) of Se p states at G point in Fig. 3c. In the monolayer, the p_z states are distant from the Fermi level, resulting in an energy difference of approximately 0.85 eV between the p_z and p_y states with different occupations (Fig. 3a and the upper panel of Fig. 3c). In the bilayer, the interfacial Se p orbitals overlap and hybridize into bonding (p_z -b-2d) and antibonding (p_z -a-2d) states to release Pauli/Coulomb repulsions (Fig. 3d), significantly splitting the p_z bands. This reduces the energy differences between p_z and p_y states around Fermi level with different occupation to 0.1 eV at G point (Fig. 3b and the lower panel of Fig. 3c), thereby enhancing p_z - p_y interactions and increasing MAE contribution favoring the z axis (Fig. 2d).

We also explored the possibility that the differences in Kitaev interactions in the mono- and bi-layer MnSe₂ might modulate the magnetic easy-axis direction. However, as listed in Appendix C, the non-collinear spin exchange and Kitaev interactions are at least two orders of magnitude weaker than that of the isotropic spin exchange coupling J_1 and remain nearly unchanged with increasing the number of layers, indicating their negligible influence on the magnetic easy-axis direction in MnSe₂ mono- and few-layers.

Furthermore, we found that monolayer and bilayer MnSe₂ are topologically nontrivial semimetals. We term the three energy bands crossing the Fermi level as band $N-1$, band N and band $N+1$, respectively (Appendix H). Forming interlayer bonding

states directly modifies band structures near the Fermi level, while layer-number-induced easy-axis rotation changes the magnetic group from P-1.1 in the monolayer to P-3m'1 in the bilayer, collectively leading to layer-number-tunable Chern numbers and surface states. (Table 2 and Fig. 3(e-f)). Both magnetic anisotropy and topological properties are governed by the bands around the Fermi level, suggesting possible magnetic-field-manipulated topological features. In addition to layer stacking, applying a vertical magnetic field can also reorient the magnetic moments in the monolayer from the easy axis to the z -axis, thereby altering the band structures and magnetic group (from P-1.1 to P-3m'1). This shift results in variations in the topological Chern numbers of the three non-trivial bands (Appendix H and Table 2), similar to what is observed in CeX (X=Cl, Br, I) [56].

Table 2 Chern numbers of MnSe₂ in 1L and 2L with different numbers of occupied bands and directions of magnetic moments.

Layer Number		1L		2L
Direction		Easy Axis	z	Easy Axis(z)
<i>Band No.</i>	$N+1$	-4	-2	2
	N	0	0	0
	$N-1$	0	-4	-5

C. Modulation of the easy axis direction in MnSe₂ monolayer

In addition to the magnetic field, stacking orders, charge doping and external strain can also effectively change the electron band structure around the Fermi level and thus the easy axis direction. Besides the most stable AA stacking, we considered five additional stacking orders and demonstrated that the interlayer stacking can effectively control the magnetic ground state and easy-axis direction (Appendix D) [28]. The AB stacking configuration (Fig. 4(a)) shares the same FM groundstate with AA stacking but exhibits a different in-plane easy-axis. To understand how stacking order rotates the orientation of the easy axis, we plotted the contributions of different atoms to the MAE of both AA and AB stacked bilayers (Fig. 4(b)). In the transition from AA to AB

stacking, there is no qualitative change in the favored easy-axis direction of different atoms, but the MAE contribution of the Se-interface decreases significantly by threefold, while the contribution of the Se-surface nearly doubles. As a result, the reduced MAE contribution of the Se-interface becomes less competitive compared to that of the Se-surface, leading to an in-plane easy axis in the AB stacked bilayer. This change in the Se-interface MAE contribution arises from the weakened interaction between the p_z and p_y states (Appendix I).

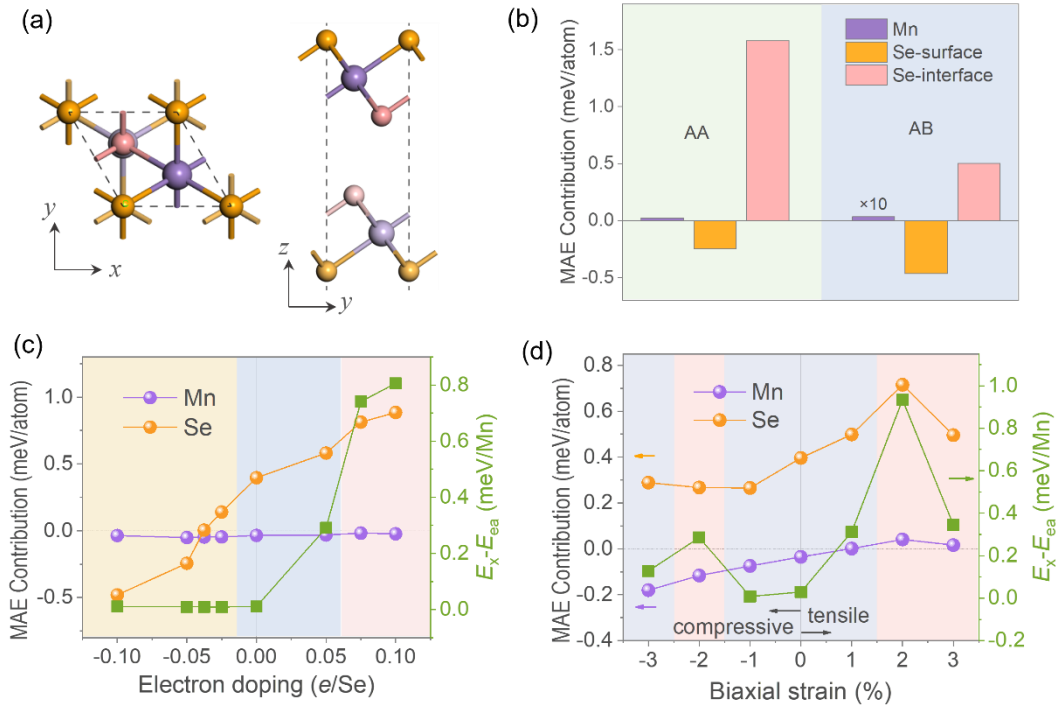


Fig. 4 Modulation of the magnetic anisotropy of MnSe₂. (a) Structure model of AB stacked bilayer. (b) Atomically decomposed MAE of AA and AB stacking. (c-d) Atomically decomposed MAE and the energy difference required to reorient the magnetic moments from the easy axis (E_{ea}) to the x axis (E_x) as a function of doping concentrations(c) and in-plane biaxial strain(d) in monolayer MnSe₂. The light brown, blue, and pink shading indicate that the easy axis lies in the xy -plane, tilts away from the z -axis, and aligns with the z -axis, respectively.

Charge doping and in-plane strain are commonly introduced by substrates. They are often employed to manipulate the magnetism of 2D magnets. Therefore, we

considered the influence of charge doping and in-plane strain on the magnetic anisotropy of monolayer MnSe_2 . By varying doping concentrations (Fig. 4c) and applying biaxial strain (Fig. 4d), the orientations of the easy axis of monolayer MnSe_2 can be manipulated. When the doping concentration is adjusted to either -0.05 or 0.075 e/Se, or when biaxial strain reaches -2% or 2%, the easy axis undergoes a rotation towards the xy -plane or z -axis (Appendix I), showcasing the adjustability of the easy axis in monolayer MnSe_2 . The atomically decomposed MAE in Fig. 4c,d reveals that the MAE contribution of Se exhibits significant variability, whereas Mn consistently makes relatively minor contributions, corroborating earlier findings.

Finally, to further support the importance of non-metallic atoms in orientating the easy axis, we substituted the Se atoms with Te atoms and studied the magnetic anisotropy of monolayer 1T- MnTe_2 . The 1T- MnTe_2 exhibits a large out-of-plane magnetic anisotropy with a MAE value of 1.6 meV/Mn, where the contribution from Te (1.7 meV/atom favoring the z -axis) is much larger than that from Mn (-0.3 meV/atom). The difference in the easy-axis and MAE between MnSe_2 and MnTe_2 again demonstrates the substantial contributions of nonmetallic atoms on tuning magnetic anisotropy in MnX_2 .

IV. CONCLUSIONS

In summary, we found that MnSe_2 is ferromagnetic topological semimetal, with its easy-axis direction and topological properties highly dependent on the electronic band structure near the Fermi level. By analyzing atomically and orbitally decomposed MAE and electronic structures, we revealed the mechanism by which interlayer coupling changes the direction of the easy-axis from 67° off the z -axis in the monolayer to the z -axis in the bilayer. In MnSe_2 , the electronic states near the Fermi level are mainly contributed by non-metallic Se atoms, resulting in the significant influence of interlayer coupling between interfacial Se atoms on the electronic band structure. From the monolayer to bilayer, p_z orbitals of Se are split towards the Fermi level due to interlayer coupling, leading to the pronounced p_z - p_y interaction and MAE contribution

favoring z -axis. Furthermore, based on the modification of Se electronic states, we demonstrated that the orientation of the magnetic easy-axis can also be manipulated by stacking orders, doping, biaxial strain and substitution of non-metallic atoms. Our results advance the understanding of the mechanism behind the rotation of the easy axis orientation in 2D layered magnets.

ACKNOWLEDGMENTS

We thank Prof. Jun Hu at Ningbo University, Prof. Lixin He and Gan Jin at University of Science and Technology of China for valuable discussions. We gratefully acknowledge the financial support from the Ministry of Science and Technology (MOST) of China (Grant No. 2023YFA1406500), the National Natural Science Foundation of China (Grants No. 92477205, No. 52461160327, and No.12104504), the Fundamental Research Funds for the Central Universities, and the Research Funds of Renmin University of China [Grants No. 22XNKJ30 (W.J.) and 24XNKJ17 (C.W.)]. All calculations for this study were performed at high performance cluster at center for joint quantum studies (HPC-CJQS) of Tianjin University, the Physics Lab of High-Performance Computing (PLHPC) and the Public Computing Cloud (PCC) of Renmin University of China.

APPENDIX A: EFFECTS OF FUNCTIONAL AND DIFFERENT U-VALUES ON THE GEOMETRY AND MAGNETIC GROUND STATE OF MONOLAYER MnSe₂

Table 3 Lattice Constant, magnetic moment per Mn atom and layer thickness d_l of monolayer MnSe₂ calculated with different exchange-correlation functionals. To ensure the robustness and applicability of our methods, we evaluated the equilibrium lattice constants of the FM configuration using different functionals, e.g., with or without various forms of vdW correction, and with or without UJ correction. We choose the PBE-D3+ UJ for structure optimization and electronic structures.

Functional	Lattice Constant(Å)	Mag.Mn(μ_B)	d_l (Å)
------------	---------------------	-------------------	-----------

PBE-w/o UJ	3.48	2.89	2.87
PBE+UJ	3.62	3.71	2.86
PBE-D2+UJ	3.57	3.67	2.90
PBE-D3+UJ	3.61	3.71	2.88
optB86b-vdw+UJ	3.56	3.60	2.88
optB88-vdw+UJ	3.59	3.62	2.88
SCAN- rVV10+UJ	3.63	4.00	2.83

Table 4 Lattice Constant, magnetic moment per Mn, layer thickness d_1 and interlayer spacing d_2 of bilayer MnSe₂ with various exchange-correlation functionals.

Functional	Lattice Constant(Å)	Mag.Mn(μ_B)	d_1 (Å)	d_2 (Å)
PBE-w/o UJ	3.48	2.89	2.75	3.26
PBE+UJ	3.65	3.78	2.85	3.00
PBE-D2+UJ	3.59	3.74	2.91	2.91
PBE-D3+UJ	3.63	3.78	2.86	2.71
optB86b-vdw+UJ	3.59	3.70	2.88	2.70
optB88-vdw+UJ	3.62	3.72	2.88	2.81
SCAN-rVV10+UJ	3.67	4.07	2.80	2.78

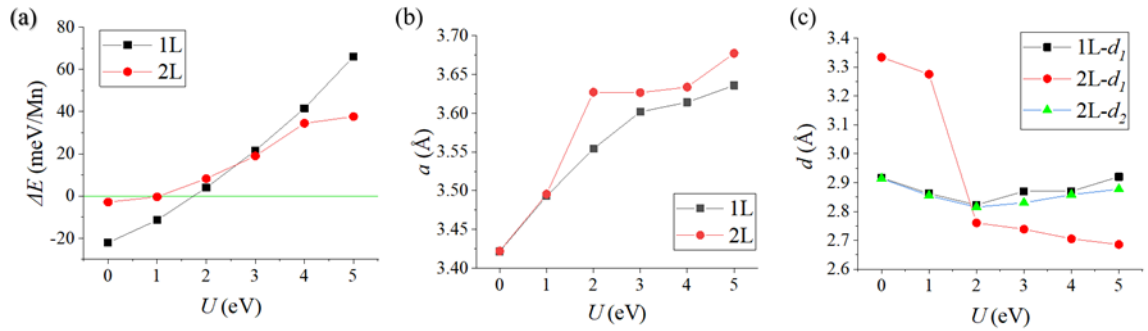


Fig. 5 (a) Energy differences between FM and AFM configurations ($\Delta E = E_{\text{AFM}} - E_{\text{FM}}$) (b) lattice constant a , and (c) thickness d_1 and interlayer spacing d_2 with respect to different U values. Here, we choose the AFM configuration with lowest energy among all AFM orders in mono- or bilayer MnSe₂ as a representative. By using the linear response method calculated U value of 4 eV, our calculations indicate the magnetic ground states and geometric structures converges and should be robust in our calculations.

APPENDIX B: MAGNETIC GROUND STATES AND HEISENBERG EXCHANGE PARAMETERS

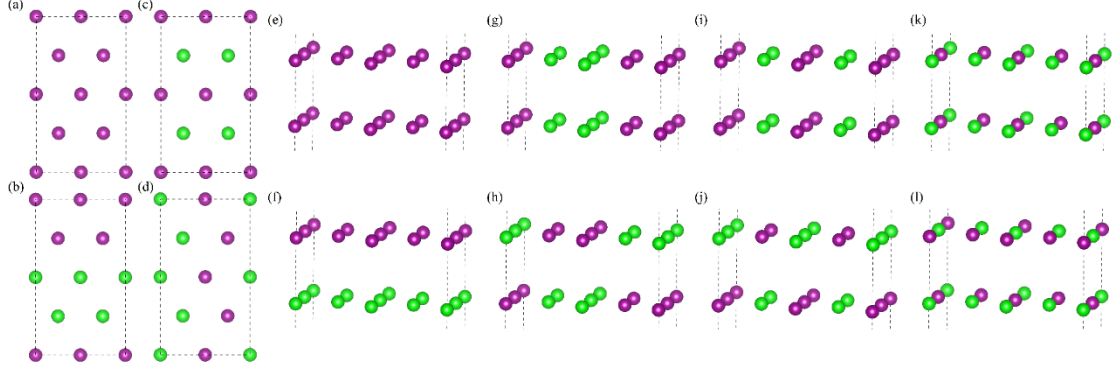


Fig. 6 Magnetic ground states and spin exchange parameters of mono-/bi-layer MnSe_2 . (a-d) Top views of schematics showing intralayer magnetic orders, including FM (a), AABB (b), ABAB (c) and ZZ (d) in monolayer/bilayer MnSe_2 , respectively. (e-l) Schematics of eight magnetic orders used for finding the magnetic groundstate and deriving spin-exchange parameters of bilayer MnSe_2 . Purple and green balls represent two anti-parallel orientations of magnetic moments on Mn atoms, respectively.

Magnetic energies of these magnetic configurations in each magnetic unit cell read as follow:

$$\begin{aligned}
 E_e &= -\frac{N^2}{4} \times \frac{1}{2} \left(6J_1 + 6J_2 + 6J_3 + \frac{1}{2}J_4 + 3J_5 + 3J_6 \right) + E_0 \\
 E_f &= -\frac{N^2}{4} \times \frac{1}{2} \left(6J_1 + 6J_2 + 6J_3 - \frac{1}{2}J_4 - 3J_5 - 3J_6 \right) + E_0 \\
 E_g &= -\frac{N^2}{4} \times \frac{1}{2} \left(2J_1 - 2J_2 - 2J_3 + \frac{1}{2}J_4 + J_5 - J_6 \right) + E_0 \\
 E_h &= -\frac{N^2}{4} \times \frac{1}{2} \left(2J_1 - 2J_2 - 2J_3 - \frac{1}{2}J_4 - J_5 + J_6 \right) + E_0 \\
 E_i &= -\frac{N^2}{4} \times \frac{1}{2} \left(-2J_1 - 2J_2 + 6J_3 + \frac{1}{2}J_4 - J_5 - J_6 \right) + E_0 \\
 E_j &= -\frac{N^2}{4} \times \frac{1}{2} \left(-2J_1 - 2J_2 + 6J_3 - \frac{1}{2}J_4 + J_5 + J_6 \right) + E_0 \\
 E_k &= -\frac{N^2}{4} \times \frac{1}{2} \left(-2J_1 + 2J_2 - 2J_3 + \frac{1}{2}J_4 - J_5 + J_6 \right) + E_0 \\
 E_l &= -\frac{N^2}{4} \times \frac{1}{2} \left(-2J_1 + 2J_2 - 2J_3 + \frac{1}{2}J_4 + J_5 - 3J_6 \right) + E_0
 \end{aligned}$$

where N represents the unpaired spins on each Mn atom, which is treated as 3 in

our exchange parameter calculations, and E_0 represents the energy that is independent of the magnetic configuration.

Table 5 Relative total energies of mono-/bi-layer MnSe₂ in different magnetic configurations shown in Fig. 6. The term “Mag. Config.” is the abbreviation of magnetic configuration. We set the total energy of the FM(-FM) configuration as the reference zero.

Layer Number	Mag. Config.	ΔE (meV/Mn)
Monolayer	FM	0.0
	AABB	42.0
	ABAB	77.7
	ZZ	70.3
bilayer	FM-FM	0.0
	FM-AFM	31.4
	AABB-FM	62.1
	AABB-AFM	72.4
	ABAB-FM	100.4
	ABAB-AFM	94.9
	ZZ-FM	102.4
	ZZ-AFM	108.1

APPENDIX C: ANISOTROPIC SPIN EXCHANGE PARAMETERS AND KITAEV INTERACTIONS

To investigate the effects of non-collinear spin exchange and Kitaev interactions on magnetic anisotropy, we considered an anisotropic Hamiltonian containing both anisotropic spin exchange coupling (SEC) and single ion anisotropy(SIA) terms:

$$H = H_{EX} + H_{SIA} = -\frac{1}{2} \left[\sum_{i \neq j} \mathbf{S}_i \cdot \mathbf{J}_{ij} \cdot \mathbf{S}_j + 2 \sum_i \mathbf{S}_i \cdot \mathbf{A} \cdot \mathbf{S}_i \right]$$

where \mathbf{J}_{ij} is the anisotropic Heisenberg exchange parameter matrix and \mathbf{A} is a vector

representing the single-ion anisotropy. We assume that J_{ij} is symmetric and $\mathbf{A}_y=0$. Following the methodology outlined in our previous research [43,57], we derived the parameters and transformed the J_{ij} matrix into the coordinate system $\{\alpha\beta\gamma\}$, corresponding to the Mn-Se bond directions. The resulting J_{ij} matrix is:

$$J_{ij} = \begin{pmatrix} 8.73 & -0.02 & 0.04 \\ -0.02 & 8.76 & 0.05 \\ 0.04 & 0.05 & 8.66 \end{pmatrix}$$

for the monolayer, and:

$$J_{ij} = \begin{pmatrix} 11.47 & 0.02 & 0.08 \\ 0.02 & 11.51 & 0.02 \\ 0.08 & 0.02 & 11.47 \end{pmatrix}$$

for the bilayer.

Because the nondiagonal elements are negligible in J_{ij} , we can express the H_{EX} as:

$$H_{EX} = -\frac{1}{2} \sum_{i \neq j} (\lambda_\alpha \mathbf{s}_i^\alpha \mathbf{s}_j^\alpha + \lambda_\beta \mathbf{s}_i^\beta \mathbf{s}_j^\beta + \lambda_\gamma \mathbf{s}_i^\gamma \mathbf{s}_j^\gamma) = -\frac{1}{2} \sum_{i \neq j} (J \mathbf{s}_i \cdot \mathbf{s}_j + K \mathbf{s}_i^\gamma \mathbf{s}_j^\gamma)$$

where $J = (\lambda_\alpha + \lambda_\beta)/2$ represent the isotropic nearest-neighbor exchange coupling in the $\alpha\beta$ -plane and $K = \lambda_\alpha - J$ is the Kitaev anisotropic nearest-neighbor exchange coupling parameter. Using these formulations, we can calculate the values of J and K for both monolayer and bilayer, as listed in Table 6.

Table 6 J and K in monolayer and bilayer MnSe₂.

Layer Number	J (meV/Mn)	K (meV/Mn)
1L	8.75	0.11
2L	11.47	0.04

APPENDIX D: STACKING ORDER TUNABLE MAGNETIC GROUND STATES AND EASY-AXIS DIRECTIONS

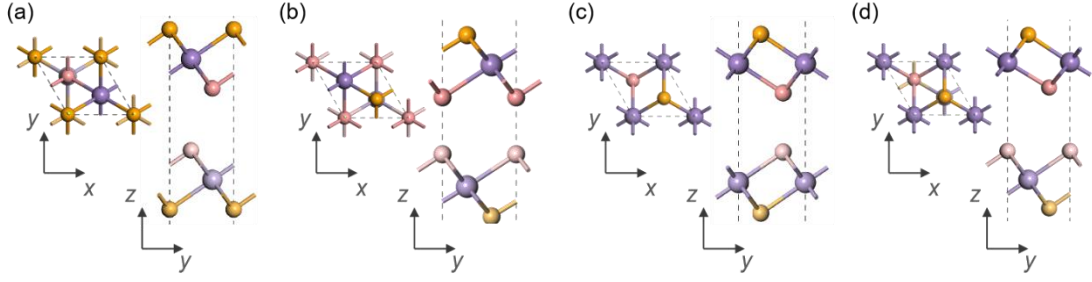


Fig 7 Structure models of bilayer MnSe_2 in AB(a), AC(b), AA^{R} (c) and AB^{R} (d) stacking orders. We consider several common stacking orders in TMD materials [28]. As shown in Table 7, We found AA stracking is most energetically favored among all considered stacking orders with an energy difference of at least 4 meV/Mn. Stacking orders can effectively mudulated the interlayer magneitic groud states (AC and AA^{R} stacking) and easy axis direction (AB stacking).

Table 7. Magnetic properties and relative energy of bilayer MnSe_2 of stacking orders.

Stacking	Magnetic Ground State	E (meV/Mn)	Easy Axis	MAE (meV/Mn)
AA	FM-FM	0	Out of Plane	0.6
AB	FM-FM	18	In Plane	0.1
AC	FM-AFM	11	Out of Plane	2.9
AA^{R}	FM-AFM	20	Out of Plane	1.5
AB^{R} (same as AC^{R})	FM-FM	4	Out of Plane	0.7

APPENDIX E: K-MESH DEPENDENCE OF MAE CALCULATIONS

The magnetic anisotropy energy (MAE) is highly sensitive to the choice of k -mesh. To ensure the accuracy of our calculations, we performed extensive convergence tests on the k -mesh using the more accurate tetrahedron method with Blöchl corrections for total energy calculations. As shown in Fig. 8, $E_x - E_z$ converges to 0.01 meV/Mn for both the monolayer and bilayer when the k -mesh is set to 29×29 . For atomically and orbitally decomposed MAE contributions, the k -point convergence is even better. These results ensure the robustness of the conclusions presented in our study.

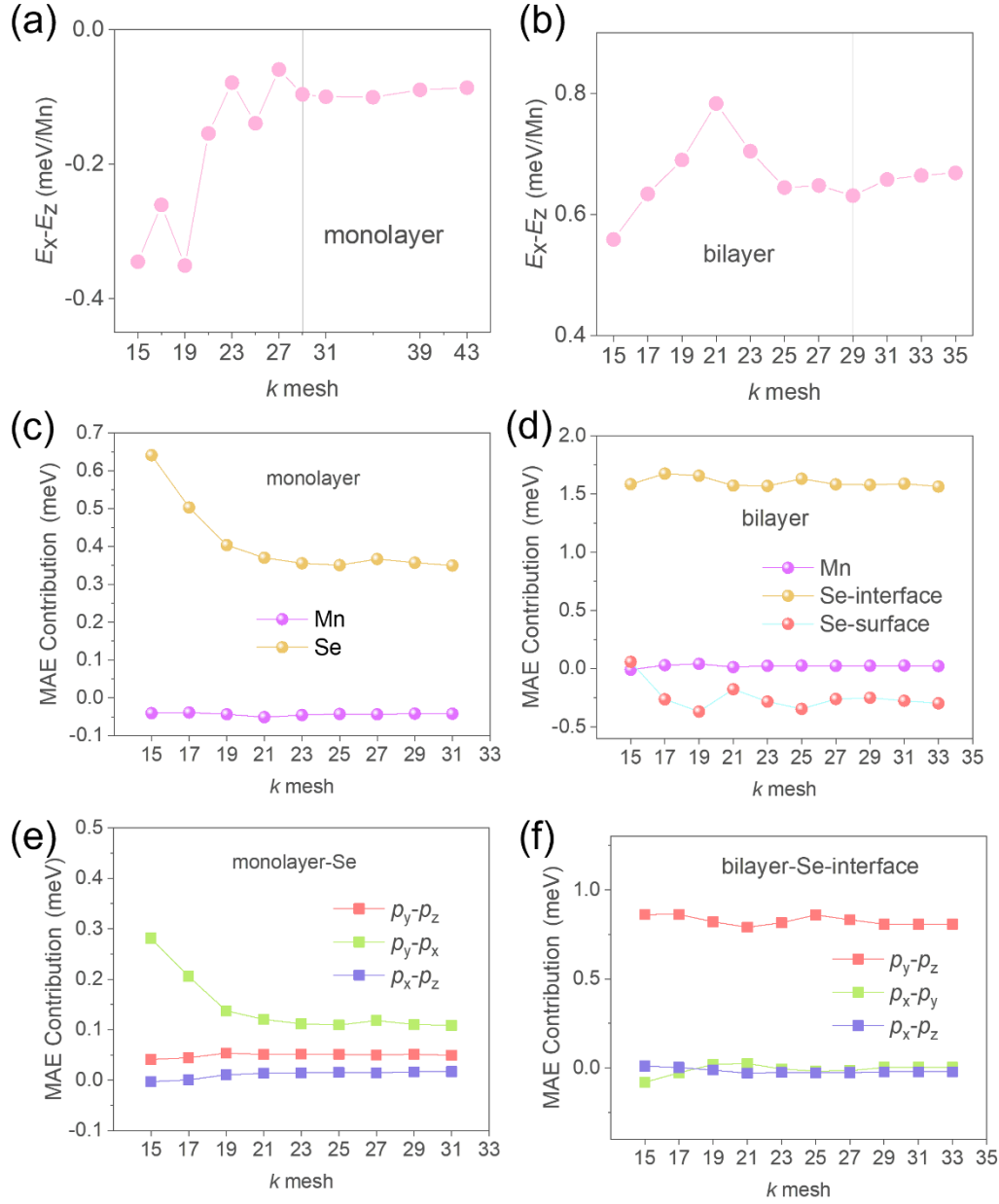


Fig.8 (a-b) Energy difference with respect to k -mesh in monolayer (a) and bilayer (b), where E_x , E_z , represent the energy of the magnetic moment along the directions of x and z axis. (c-f) K -mesh dependence of atomically and orbitally decomposed MAE contributions.

APPENDIX F: ORBITAL-RESOLVED MAE CONTRIBUTIONS

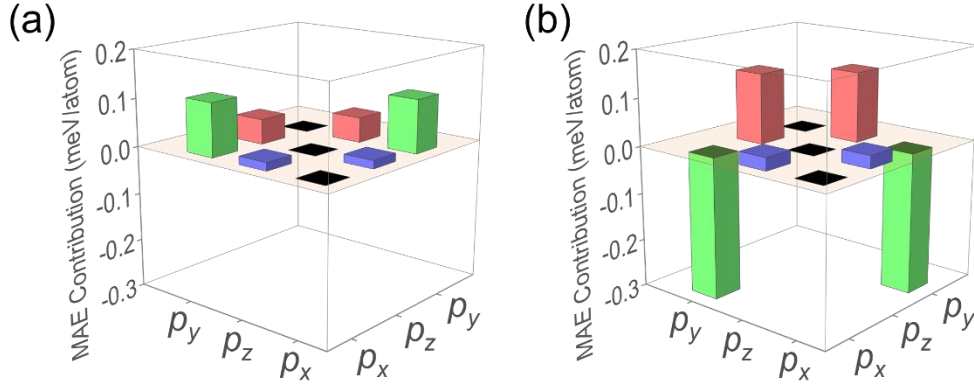


Fig. 9 Orbital-resolved MAE contribution of Se in monolayer(a) and Se-surface in bilayer(b).

APPENDIX G: ELECTRONIC STRUCTURES WITH ORBITAL DECOMPOSITION

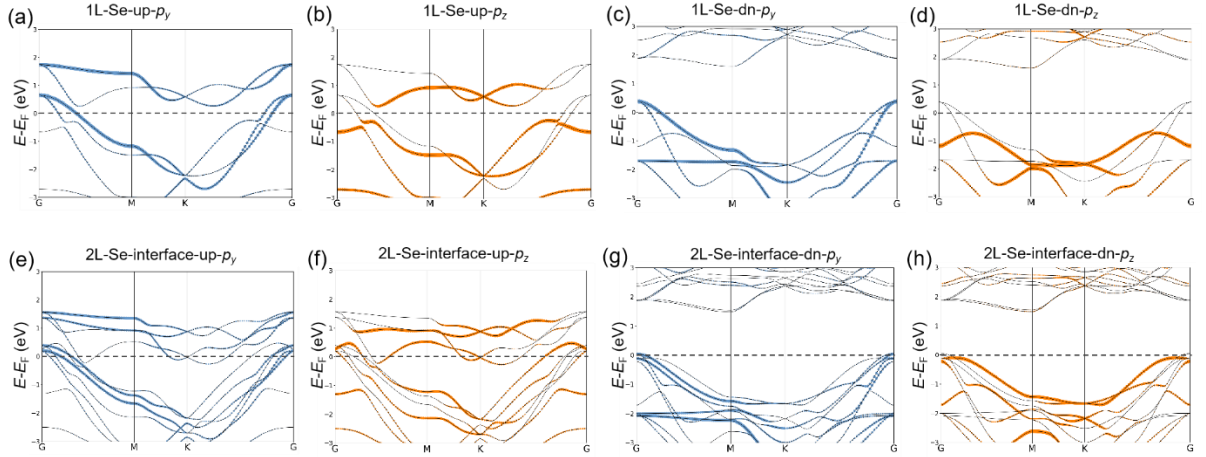


Fig. 10 Band structures of monolayer(a-d) and bilayer(e-h) MnSe₂. The (interfacial) Se p_z and p_y orbitals are mapped with different colors: orange, p_z ; blue, p_y .

The states and their contributions to MAE can be related through the second-order perturbation theory [55]:

$$MAE = \sum_{u,o} \frac{|\langle u | H_{SOC}(x) | o \rangle|^2 - |\langle u | H_{SOC}(z) | o \rangle|^2}{E_o - E_u}$$

where o and u correspond to occupied and unoccupied states, respectively. The energy differences between occupied and unoccupied states ($E_o - E_u$) are in the denominator,

indicating that states near the Fermi level have a greater influence on the MAE compared to those further away.

APPENDIX H: BAND STRUCTURES WITH THE INCLUSION OF SPIN-ORBIT COUPLING

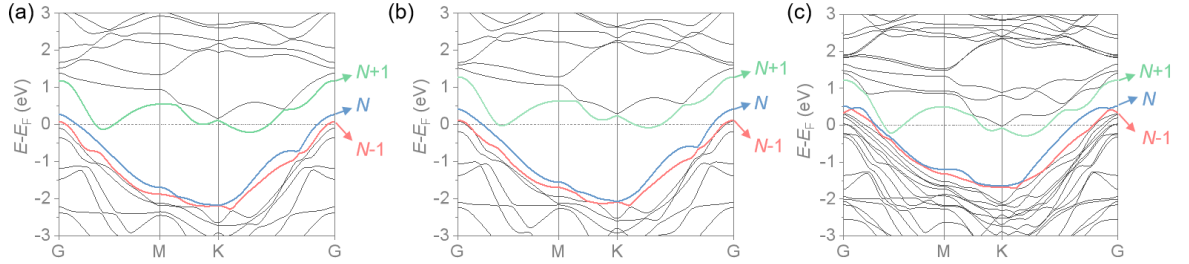


Fig. 11 (a-b) Band structures of monolayer(a,b) and (c) bilayer MnSe₂ with SOC, while the magnetic moment is along the easy axis of the monolayer in (a) and along the z-axis in (b,c). The symbols $N-1$, N , $N+1$ denote bands with respective colors.

APPENDIX I: EFFECTS OF DOPING, STRAIN, AND STACKING ORDERS ON EASY AXIS DIRECTION

Table 8 Lattice constants, easy axis direction and magnetic anisotropic energies of monolayer MnSe₂ upon electron/hole doping. FM remains the ground state at different doping concentrations.

Electron doping(e/Se)	Lattice Constant (Å)	Easy Axis		
		$\theta(^{\circ})$	$\phi(^{\circ})$	$E_x - E_{ea}$ (meV/Mn)
-0.1	3.58	90	90	0.01
-0.05	3.60	90	116	0.01
-0.0375	3.61	89	116	0.01
-0.025	3.61	90	112	0.01
0	3.61	68	111	0.01
0.05	3.61	17	96	0.29
0.075	3.61	0	90	0.74
0.1	3.63	0	90	0.81

Table 9 Lattice constants, easy axis directions and magnetic anisotropic energies of monolayer MnSe₂ under biaxial strain. FM remains the ground state under strain.

Strain (%)	Lattice Constant (Å)	Easy Axis		
		$\theta(^{\circ})$	$\phi(^{\circ})$	$E_x - E_{ea}$ (meV/Mn)
-3	3.50	15	34	0.13
-2	3.54	0	90	0.29
-1	3.57	90	114	0.01
0	3.61	68	111	0.01
1	3.65	16	109	0.31
2	3.68	0	90	0.93
3	3.72	0	90	0.35

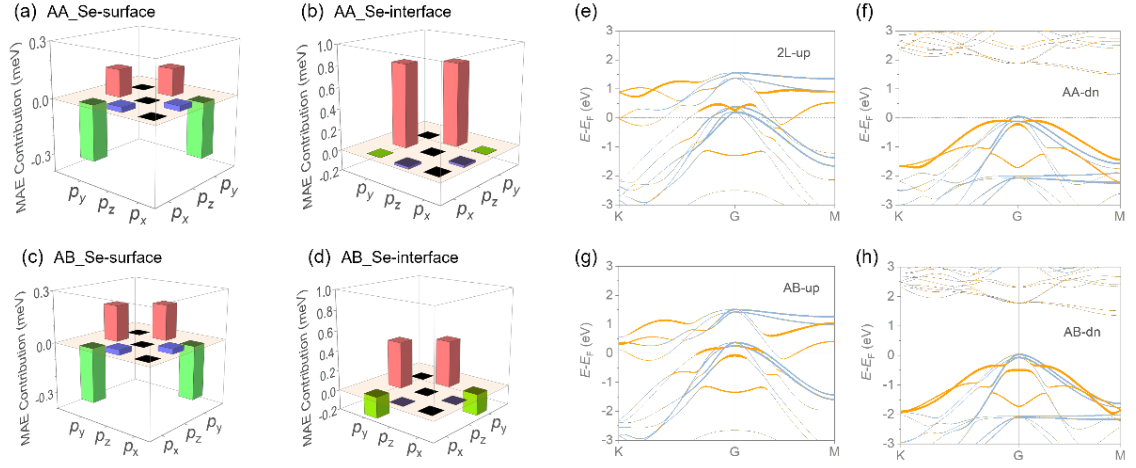


Fig. 12 Orbital-resolved MAE contribution of Se in AA(a-b) and AB(c-d) stacking. (e-h) Band structures of AA(e-f) and AB(g-h) stacked bilayer MnSe_2 . The selected p_z and all p_y orbitals of (interfacial) Se are mapped with different colors: orange, p_z ; light blue, p_y . The Fermi level is marked using grey dot dash line. From the orbital-resolved MAE in (a-d), we found that the most notable difference between AA and AB stacking lies in the weakened interaction between p_z and p_y states in AB stacking. This change arises from the shift of p_z states in AB stacked bilayer.

- [1] Q. H. Wang et al., The Magnetic Genome of Two-Dimensional van der Waals Materials, *ACS Nano* **16**, 6960 (2022).
- [2] Nan-Shu L., Cong W., and Wei J., Recent research advances in two-dimensional magnetic materials, *Acta Phys. Sin.* **71**, 127504 (2022).
- [3] B. Huang et al., Layer-dependent ferromagnetism in a van der Waals crystal down to the monolayer limit, *Nature* **546**, 270 (2017).
- [4] C. Gong et al., Discovery of intrinsic ferromagnetism in two-dimensional van der Waals crystals, *Nature* **546**, 265 (2017).
- [5] B. Zhou, S. Ji, Z. Tian, W. Cheng, X. Wang, and W. Mi, Proximity effect induced spin filtering and gap opening in graphene by half-metallic monolayer Cr₂C ferromagnet, *Carbon* **132**, 25 (2018).
- [6] C. Gong and X. Zhang, Two-dimensional magnetic crystals and emergent heterostructure devices, *Science* **363**, eaav4450 (2019).
- [7] W. Vreugdenhil, J. G. Haasnoot, O. Kahn, P. Thuery, and J. Reedijk, A copper(II) dope as a detector for the high-spin to low-spin transition in the two-dimensional compound [trans-bis(thiocyanato)bis(4,4'-bi-1,2,4-triazole)iron] hydrate, *J. Am. Chem. Soc.* **109**, 5272 (1987).
- [8] W. Liu, X. Bao, J.-Y. Li, Y.-L. Qin, Y.-C. Chen, Z.-P. Ni, and M.-L. Tong, High-Temperature Spin Crossover in Two Solvent-Free Coordination Polymers with Unusual High Thermal Stability, *Inorg. Chem.* **54**, 3006 (2015).
- [9] G. Chakraborty, I.-H. Park, R. Medishetty, and J. J. Vittal, Two-Dimensional Metal-Organic Framework Materials: Synthesis, Structures, Properties and Applications, *Chem. Rev.* **121**, 3751 (2021).
- [10] J.-J. Xian et al., Spin mapping of intralayer antiferromagnetism and field-induced spin reorientation in monolayer CrTe₂, *Nat Commun* **13**, 257 (2022).
- [11] K. S. Burch, D. Mandrus, and J.-G. Park, Magnetism in two-dimensional van der Waals materials, *Nature* **563**, 47 (2018).
- [12] F. Yao, V. Multian, Z. Wang, N. Ubrig, J. Teyssier, F. Wu, E. Giannini, M. Gibertini, I. Gutiérrez-Lezama, and A. F. Morpurgo, Multiple antiferromagnetic phases and magnetic anisotropy in exfoliated CrBr₃ multilayers, *Nat Commun* **14**, 4969 (2023).
- [13] Q. Cui, L. Wang, Y. Zhu, J. Liang, and H. Yang, Magnetic anisotropy, exchange coupling and Dzyaloshinskii–Moriya interaction of two-dimensional magnets, *Front. Phys.* **18**, 13602 (2023).
- [14] Y. Wang et al., Strain-Sensitive Magnetization Reversal of a van der Waals Magnet, *Advanced Materials* **32**, 2004533 (2020).
- [15] D. Chiba, M. Sawicki, Y. Nishitani, Y. Nakatani, F. Matsukura, and H. Ohno, Magnetization vector manipulation by electric fields, *Nature* **455**, 515 (2008).
- [16] I. M. Miron, K. Garello, G. Gaudin, P.-J. Zermatten, M. V. Costache, S. Auffret, S. Bandiera, B. Rodmacq, A. Schuhl, and P. Gambardella, Perpendicular switching of a single ferromagnetic layer induced by in-plane current injection, *Nature* **476**, 189 (2011).
- [17] M. Tsujikawa and T. Oda, Finite Electric Field Effects in the Large Perpendicular Magnetic Anisotropy Surface $\text{Pt}/\text{Fe}/\text{Pt}(001)$: A First-Principles Study, *Phys. Rev. Lett.* **102**, 247203 (2009).

- [18] B. Rana and Y. Otani, Towards magnonic devices based on voltage-controlled magnetic anisotropy, *Commun Phys* **2**, 1 (2019).
- [19] C.-G. Duan, J. P. Velev, R. F. Sabirianov, Z. Zhu, J. Chu, S. S. Jaswal, and E. Y. Tsymbal, Surface Magnetoelectric Effect in Ferromagnetic Metal Films, *Phys. Rev. Lett.* **101**, 137201 (2008).
- [20] I. A. Verzhbitskiy, H. Kurebayashi, H. Cheng, J. Zhou, S. Khan, Y. P. Feng, and G. Eda, Controlling the magnetic anisotropy in Cr₂Ge₂Te₆ by electrostatic gating, *Nat Electron* **3**, 460 (2020).
- [21] S. Jiang, L. Li, Z. Wang, K. F. Mak, and J. Shan, Controlling magnetism in 2D CrI₃ by electrostatic doping, *Nature Nanotech* **13**, 549 (2018).
- [22] S. Jiang, J. Shan, and K. F. Mak, Electric-field switching of two-dimensional van der Waals magnets, *Nature Mater* **17**, 406 (2018).
- [23] Y.-Y. Sun, L.-Q. Zhu, Z. Li, W. Ju, S.-J. Gong, J.-Q. Wang, and J.-H. Chu, Electric manipulation of magnetism in bilayer van der Waals magnets, *J. Phys.: Condens. Matter* **31**, 205501 (2019).
- [24] T. Song et al., Switching 2D magnetic states via pressure tuning of layer stacking, *Nat. Mater.* **18**, 1298 (2019).
- [25] T. Li et al., Pressure-controlled interlayer magnetism in atomically thin CrI₃, *Nat. Mater.* **18**, 1303 (2019).
- [26] B. Huang, M. A. McGuire, A. F. May, D. Xiao, P. Jarillo-Herrero, and X. Xu, Emergent phenomena and proximity effects in two-dimensional magnets and heterostructures, *Nat. Mater.* **19**, 1276 (2020).
- [27] X. Liu et al., Tunable spin-polarized correlated states in twisted double bilayer graphene, *Nature* **583**, 221 (2020).
- [28] W. Zhu, C. Song, Y. Zhou, Q. Wang, H. Bai, and F. Pan, Insight into interlayer magnetic coupling in 1 T -type transition metal dichalcogenides based on the stacking of nonmagnetic atoms, *Phys. Rev. B* **103**, 224404 (2021).
- [29] P. Jiang, C. Wang, D. Chen, Z. Zhong, Z. Yuan, Z.-Y. Lu, and W. Ji, Stacking tunable interlayer magnetism in bilayer CrI₃, *Phys. Rev. B* **99**, 144401 (2019).
- [30] C. Wang, X. Zhou, Y. Pan, J. Qiao, X. Kong, C.-C. Kaun, and W. Ji, Layer and doping tunable ferromagnetic order in two-dimensional CrS₂ layers, *Phys. Rev. B* **97**, 245409 (2018).
- [31] A. Avsar, A. Ciarrocchi, M. Pizzochero, D. Unuchek, O. V. Yazyev, and A. Kis, Defect induced, layer-modulated magnetism in ultrathin metallic PtSe₂, *Nat. Nanotechnol.* **14**, 674 (2019).
- [32] J. Shang, X. Tang, X. Tan, A. Du, T. Liao, S. C. Smith, Y. Gu, C. Li, and L. Kou, Stacking-Dependent Interlayer Magnetic Coupling in 2D CrI₃/CrGeTe₃ Nanostructures for Spintronics, *ACS Appl. Nano Mater.* **3**, 1282 (2020).
- [33] X. Zhang et al., Room-temperature intrinsic ferromagnetism in epitaxial CrTe₂ ultrathin films, *Nat Commun* **12**, 2492 (2021).
- [34] L. Meng et al., Anomalous thickness dependence of Curie temperature in air-stable two-dimensional ferromagnetic 1T-CrTe₂ grown by chemical vapor deposition, *Nat Commun* **12**, 809 (2021).
- [35] B. Yang et al., Magnetic anisotropy reversal driven by structural symmetry-breaking in

- monolayer α -RuCl₃, Nat. Mater. **22**, 1 (2023).
- [36] J. L. Lado and J. Fernández-Rossier, On the origin of magnetic anisotropy in two dimensional CrI₃, 2D Mater. **4**, 035002 (2017).
 - [37] D. Soriano, M. I. Katsnelson, and J. Fernández-Rossier, Magnetic Two-Dimensional Chromium Trihalides: A Theoretical Perspective, Nano Lett. **20**, 6225 (2020).
 - [38] Z. Wu, Z. Shen, Y. Xue, and C. Song, Strain-induced topological phase transition and enhanced Curie temperature in MnBi₂Te₄/CrI₃ heterojunction, Phys. Rev. Materials **6**, 014011 (2022).
 - [39] J. P. Perdew, K. Burke, and M. Ernzerhof, Generalized Gradient Approximation Made Simple, Phys. Rev. Lett. **77**, 3865 (1996).
 - [40] P. E. Blöchl, Projector augmented-wave method, Phys. Rev. B **50**, 17953 (1994).
 - [41] G. Kresse and J. Furthmüller, Efficient iterative schemes for ab initio total-energy calculations using a plane-wave basis set, Phys. Rev. B **54**, 11169 (1996).
 - [42] S. Grimme, J. Antony, S. Ehrlich, and H. Krieg, A consistent and accurate ab initio parametrization of density functional dispersion correction (DFT-D) for the 94 elements H-Pu, The Journal of Chemical Physics **132**, 154104 (2010).
 - [43] N. Liu, C. Wang, C. Yan, C. Xu, J. Hu, Y. Zhang, and W. Ji, Competing multiferroic phases in monolayer and few-layer NiI_2 , Phys. Rev. B **109**, 195422 (2024).
 - [44] A. I. Liechtenstein, V. I. Anisimov, and J. Zaanen, Density-functional theory and strong interactions: Orbital ordering in Mott-Hubbard insulators, Phys. Rev. B **52**, R5467 (1995).
 - [45] M. Cococcioni and S. De Gironcoli, Linear response approach to the calculation of the effective interaction parameters in the LDA+U method, Phys. Rev. B **71**, 035105 (2005).
 - [46] P. Li, X. Liu, M. Chen, P. Lin, X. Ren, L. Lin, C. Yang, and L. He, Large-scale ab initio simulations based on systematically improvable atomic basis, Computational Materials Science **112**, 503 (2016).
 - [47] M. Chen, G.-C. Guo, and L. He, Systematically improvable optimized atomic basis sets for *ab initio* calculations, J. Phys.: Condens. Matter **22**, 445501 (2010).
 - [48] G. Jin, H. Pang, Y. Ji, Z. Dai, and L. He, PYATB: An efficient Python package for electronic structure calculations using ab initio tight-binding model, Computer Physics Communications **291**, 108844 (2023).
 - [49] A. A. Mostofi, J. R. Yates, G. Pizzi, Y.-S. Lee, I. Souza, D. Vanderbilt, and N. Marzari, An updated version of wannier90: A tool for obtaining maximally-localised Wannier functions, Computer Physics Communications **185**, 2309 (2014).
 - [50] Q. Wu, S. Zhang, H.-F. Song, M. Troyer, and A. A. Soluyanov, WannierTools: An open-source software package for novel topological materials, Computer Physics Communications **224**, 405 (2018).
 - [51] W. Ji, Z.-Y. Lu, and H. Gao, Electron Core-Hole Interaction and Its Induced Ionic Structural Relaxation in Molecular Systems under X-Ray Irradiation, Phys. Rev. Lett. **97**, 246101 (2006).
 - [52] <https://gitee.com/jigroupruc/re-meaf>, (n.d.).
 - [53] W.-Q. Xie, Z.-W. Lu, C.-C. He, X.-B. Yang, and Y.-J. Zhao, Theoretical study of tunable magnetism of two-dimensional MnSe₂ through strain, charge, and defect, J. Phys.: Condens. Matter **33**, 215803 (2021).

- [54] C. Wang, X. Zhou, L. Zhou, Y. Pan, Z.-Y. Lu, X. Wan, X. Wang, and W. Ji, Bethe-Slater-curve-like behavior and interlayer spin-exchange coupling mechanisms in two-dimensional magnetic bilayers, *Phys. Rev. B* **102**, 020402 (2020).
- [55] D. Wang, R. Wu, and A. J. Freeman, First-principles theory of surface magnetocrystalline anisotropy and the diatomic-pair model, *Phys. Rev. B* **47**, 14932 (1993).
- [56] S.-Z. Li, J.-S. Si, Z. Yang, and W.-B. Zhang, Weyl nodal loop semimetals and tunable quantum anomalous Hall states in two-dimensional ferromagnetic cerium monohalides, *Phys. Rev. B* **109**, 115418 (2024).
- [57] L. Wu, L. Zhou, X. Zhou, C. Wang, and W. Ji, In-plane epitaxy-strain-tuning intralayer and interlayer magnetic coupling in CrSe 2 and CrTe 2 monolayers and bilayers, *Phys. Rev. B* **106**, L081401 (2022).